Simulation on forming and penetrating target plate of tungsten alloy pre-fragment warhead

S Zhao[1]*, S Yuan[1], C Cheng[2], X S Shi[3], Y Fu[3], Y C Wang[4]

1. School of Equipment Engineering, Shenyang Ligong University, Shenyang Liaoning, 110159, China

2. Ningbo University, the Key Laboratory of the Ministry of Education, Impact and Safety Engineering, Ningbo, Zhejiang, 31521, China

3. No. 524 Factory, Jilin, 132021, China

4. Shanghai Research Institute of Mechanical and Electrical Engineering, Shanghai 201108, China

ABSTRACT

To study the damage ability of tungsten alloy pre-fragments warhead, its forming process is analyzed by static explosion experiment and simulation. The velocity attenuation curve of the spherical pre-fragments is obtained with a ballistic gun firing experiment, where the tungsten alloy pre-fragments penetrate the steel targets at different angles. The results show that in a certain range, the velocity attenuation of tungsten alloy pre-fragments with certain quality is slow, and the influence of air resistance is small. Compared with the theoretical formula, the error rate is also small. At the same time, the penetration angle of tungsten alloy preformed fragments is greater than 30°, which can well complete the penetration of steel targets. The penetration effect is significantly reduced when the angle is less than 30°. The results can provide a theoretical basis for the research of performed fragment warheads.

1. INTRODUCTION

Fragment killing warhead is one typical conventional warhead. Under the impact of high explosion, a large number of fragments with certain kinetic energy are formed to destroy the target. The forms of fragments can be divided into uncontrolled fragments [1], controllable fragments [2], pre-controlled fragments [3], and pre-fragments [4]. Compared with other fragment forms, prefabricated fragments are loaded into warheads. When exploding, the shape and size of fragments will be fully controlled, which can produce a better destroy effect for specific targets. The damage effect of fragments mainly includes the quality, dispersion angle, and speed of prefabricated fragments. The fragment velocity and dispersion angle would be affected by the detonation mode, the arrangement and the shape of pre-fragments [5-7]. The divergence angle directly affects the penetration angle between the fragment and the target [8-9]. Due to the formation of a large number of fragments as well as different shapes and materials of internal pre-fragments, it is difficult to predict the fragment velocity and dispersion angle. With the improvement of armor protection capability, ordinary fragments cannot penetrate the target plate, and the requirements for pre-fragments are getting higher and higher. Tungsten alloy with higher density is used for pre-fragments [10-13]. The

*Corresponding Author: zhaoqj1225@163.com

traditional experimental methods are difficult to study the formation, velocity, and dispersion angle of fragments. With the rapid development of numerical simulation methods, it is possible to predict the initial velocity and dispersion direction of fragments [14-16]. However, the experimental research on fragment velocity attenuation is rare. To this end, some experimental and numerical simulation methods are carried out to the formation of tungsten alloy-preformed fragments, the velocity attenuation of fragments, and the damage to target plates, so as to provide an important theoretical significance for the damage ability of preformed fragments.

2. MATERIALS AND METHODS

2.1. Static explosive power experiment of pre-fragment warhead

To obtain the destroy capability of the tungsten alloy pre-fragment warhead, a static explosion experiment of the pre-fragment warhead is completed. The pre-fragment warhead is shown in Fig. 1, and the static explosion experiment schematic diagram and field experiment layout are shown in Fig. 2. The experiment adopts the sector target experiment, and the target plate adopts the steel target plate. The distance between steel target plates is 6 m; the thickness of the target plates is 0.6 cm; the distance between the wooden target plates is 10 m, and the thickness of the target plates is 1.0 cm. Fig. 3 shows the bullet hole used to destroy the shaped fragment of a target plate. It can be seen that the pre-fragment warhead has optimal damage ability in a certain range. However, due to the large number of fragments, it is impossible to determine the velocity of performed fragments by conventional velocity measurement methods, and the key damage parameters such as the formation and velocity of pre-fragments are analyzed by experimental test. The finite element software is thus used to further study the performed fragment shaping, fragment velocity attenuation, and target destroy capability, so as to determine the damage capability of the pre-fragment warhead.

Fig. 1. Pre-fragment warhead

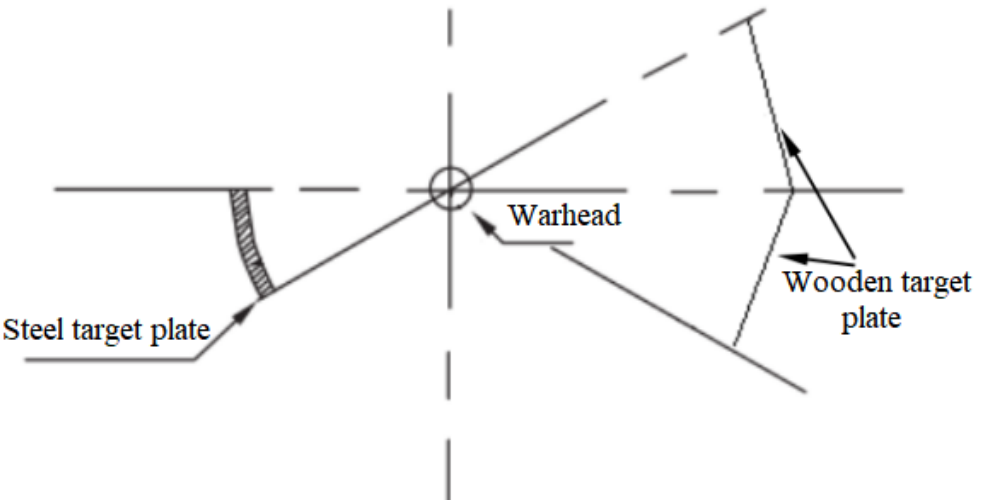

(a) Experiment diagram

(b) Field experiment layout

Fig. 2. Static explosion experiment of the pre-fragment warhead

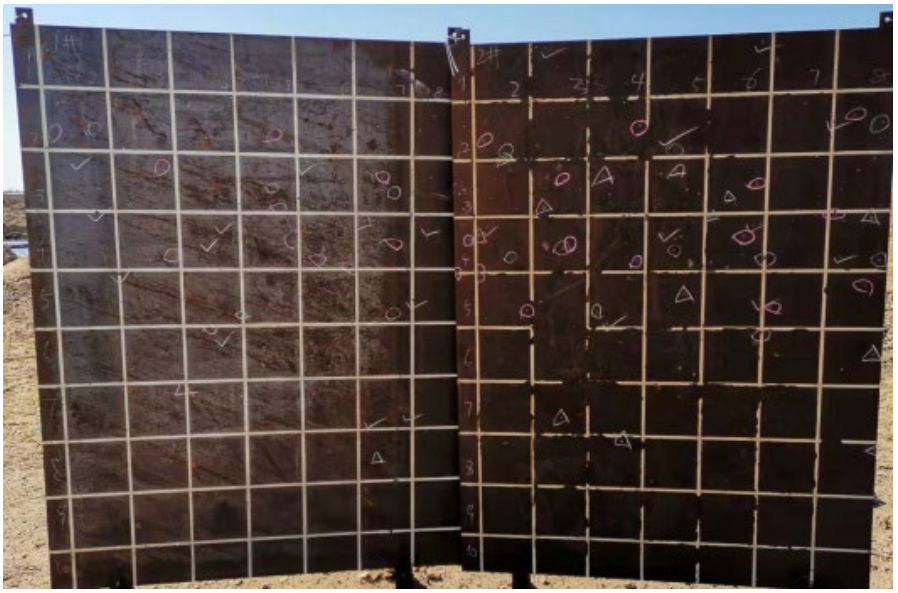

(a) Front of target plate

(b) Local magnification on the back

Fig. 3. Damage of steel target plate

2.2. Molding Process Simulation

2.2.1. Physical Model

Fig. 4 is the simulation model of an actual pre-fragment warhead, with a certain length-to-diameter ratio (D and L are the diameter and height of the warhead, respectively). The spherical performed fragment material is made of tungsten alloy, and its diameter is r. The explosive is 8701; the lining is made of 30CrMnSi steel, and the outer lining is made of aluminum alloy. The warhead in the model is simplified to a certain extent.

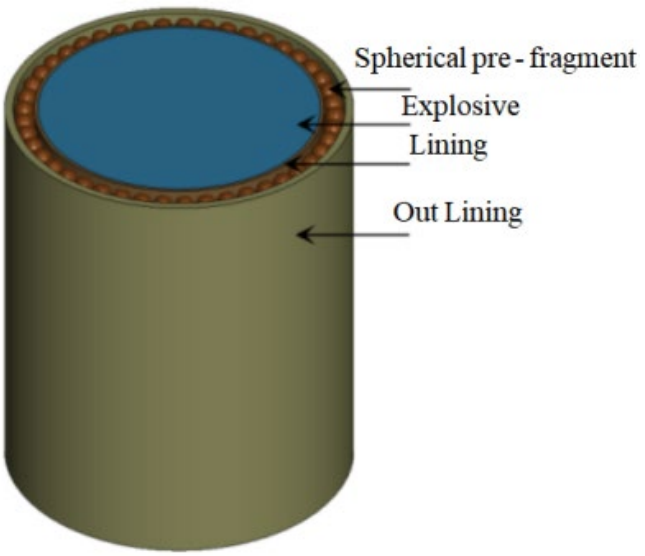

Fig. 4. Finite element model

LS-DYNA software is used to establish the finite element model [17-18]. To obtain better molding effect, an ELASTIC material model is used for tungsten alloy per-fragments. The plastic follow-up model PLATIC is used for lining and outer lining_ KINEMATIC material model, and HIGH_ EXPLOSIVE_ BURN material model. Specific parameters are shown in Table 1-3.

Table 1. Model parameters of tungsten alloy prefabricated fragment materials (cm-g- μ s)

ρ	μ	E(Gpa)
17.9	0.28	0.410

Table 2. Material parameters of 30CrMnSi Steel and LY-12cz aluminum alloy (cm-g- μ s)

	ρ	E	μ	σ_y	FS
30CrMnSi	7.80	210	0.28	0.235	0.8
LY-12cz	2.78	72	0.30	0.294	0.3

Table 3. 8701 explosive material parameters (cm-g- μ s)

ρ	D	P (Mbar)	A (Mbar)	B (Mbar)	R_1	R_2	ω	E_0 (Mbar)
1.7	0.81	0.32	4.48	0.057	4.26	1.1	0.36	0.09

8701 explosive adopts HIGH_ EXPLOSIVE_ BURN material model and JWL equation of state:

$$P = A\left(1 - \frac{\omega}{R_1 V}\right)e^{-R_1 V} + B\left(1 - \frac{\omega}{R_2 V}\right)e^{-R_2 V} + \frac{\omega E}{V} \tag{1}$$

where P is the detonation pressure; V is the relative volume; E is the internal energy per unit volume; ω, A, B, R_1 and R_2 are materials.

2.2.2. Molding process analysis

Fig. 5 is the initiation process of the pre-fragment warhead. After the explosive initiation, the warhead starts to expand under the action of detonation gas. The outer lining gradually erodes, and the velocity of pre-fragments gradually increases. The fragment velocity tends to be stable after it increases to a certain extent. At the same time, the speed of pre-fragments near the initiation point is high, and that far from the initiation point is low. As the time increases, the pre-fragments form a certain dispersion angle, whose dispersion degree gradually increases. One node is picked up every two prefabricated fragments from the top to the bottom, and the speed of pre-fragments is shown in Fig.6. The initiation point is at the height of the 357755 node. It can be seen that the velocity of pre-fragments near the initiation point is relatively high, with about 1400m/s, and that at the far initiation point is relatively low, with about 1100 m/s. Most fragment velocities are concentrated at 1350m/s. The main reason is the concentration of the energy released at the moment of explosion, and the more energy acts on the fragments. However, as the inner liner and outer liner shells break, the energy release begins to disperse and the energy acting on the fragments decreases.

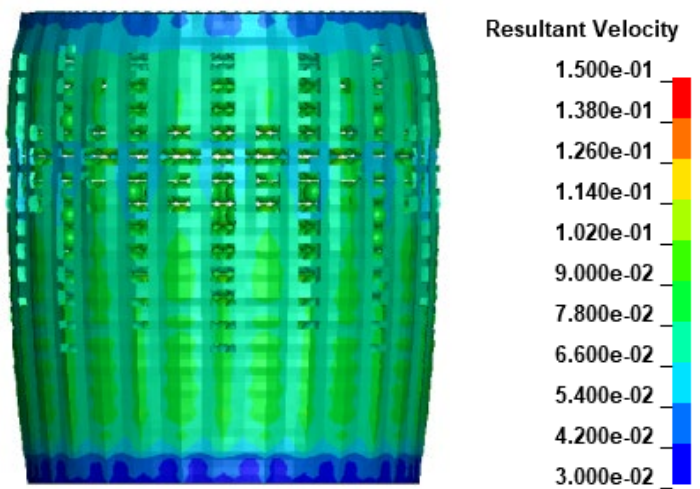

(a) 25μs

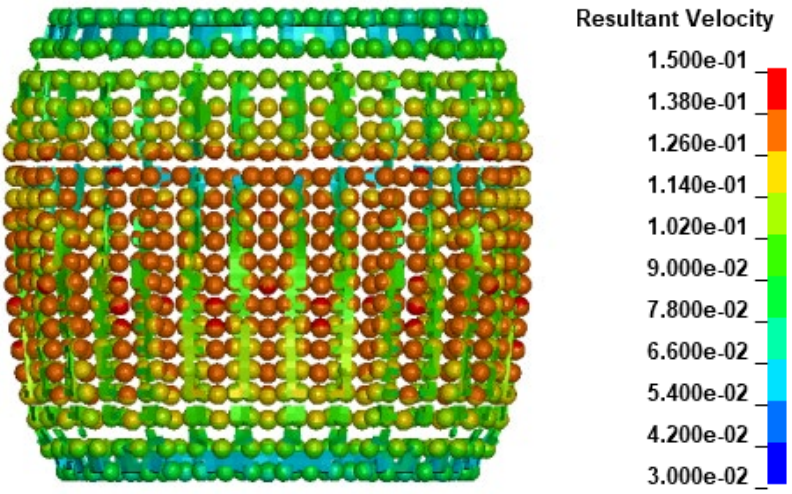

(b) 50μ

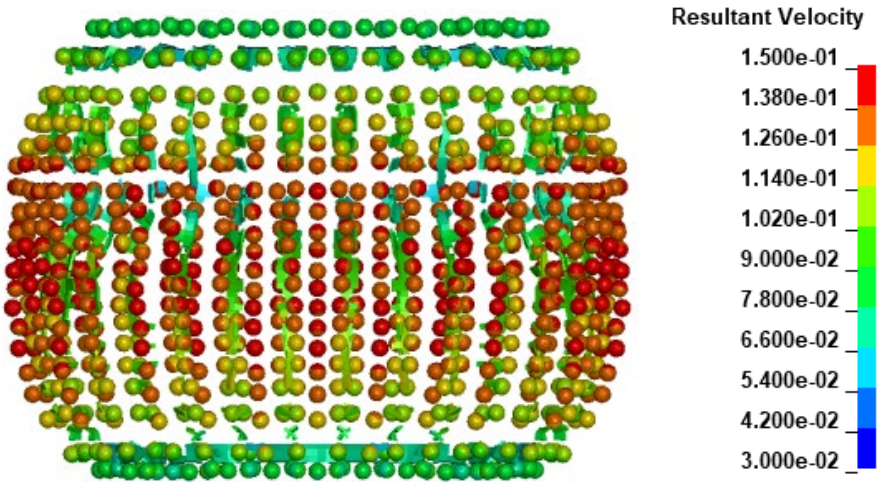

(c) 75μs

Fig. 5. Formation of pre-fragments

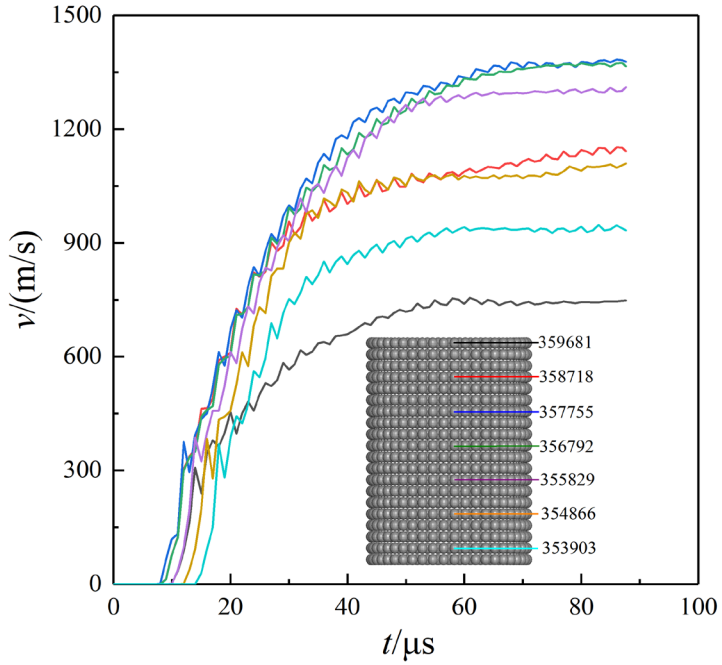

Fig. 6. Pre-fragment speed at different positions

2.2.3. Pre-fragment velocity attenuation calculation

The resistance of spherical fragments in flight is mainly air resistance [19], which can be expressed as follows:

$$F = k_d \rho_A S_f |v_p - v_{f1}|(v_p - v_{f1}) \tag{2}$$

where v_p is the fragment velocity; v_{f1} is the absolute velocity of air flow; S_f is the windward area of fragment in the flow field, and k_d is the air resistance coefficient, with a value of 0.97.

According to Newton's second law, it is obtained that:

$$m\frac{dv_p}{dt} = \frac{1}{2}k_d \rho_A S_f (v_p - v_{f1})^2 \tag{3}$$

The fragments are evenly distributed outside. Assuming that the air flow field is uniform without pressure, the air flow rate is 0, and the sectional area is S. The fragment radius R is the most important factor affecting the velocity attenuation of spherical fragments, which can be expressed as:

$$v_p = v_0 \, exp\left(-\frac{k_d \rho_A \pi r^2}{2m} X\right) = v_0 \, exp\left(-\frac{3k_d \rho_A}{8\rho_p r} X\right) \tag{4}$$

where substituting the relevant parameters of tungsten alloy pre-fragments into the formula, can obtain the attenuation of velocity of spherical pre-fragments with distance.

Since there are many pre-fragments in the warhead, the velocity of individual fragments cannot be measured by ordinary static explosion experiments. This paper uses a ballistic gun to launch a tungsten alloy spherical projectile, and the velocity of the projectile is measured by the test paper targets, so as to obtain the variation of the velocity of tungsten alloy projectiles with the specific initial velocity in a distance. The experimental arrangement is shown in Fig.7. The test target is arranged at 6-13 m, each target with a space of 1 m. From Eq. 4 and Fig.8, it can be seen that the theoretical calculation results are consistent with the test results. The tungsten alloy pre-fragments decay slowly at a short distance (within 13 m), and the influence of air resistance is small. Referring to the theoretical results, it is assumed that the target plate is located at 6 m and the velocity of pre-fragments is about 1330 m/s.

Fig. 7. Railgun experiment

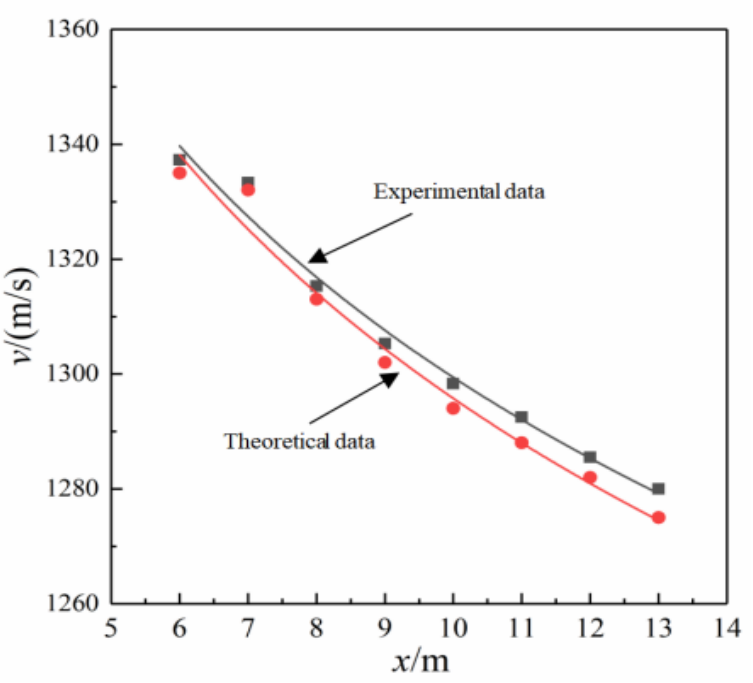

Fig. 8. Comparison of experimental and theoretical pre-fragment velocity

3. RESULTS AND ANALYSIS

3.1. Damage target simulation model

Since the pre-fragments are fan-shaped and dispersed under the action of detonation wave, the angle of penetration into the target plate is constantly changing. Thus this paper simulates the pre-fragments penetration of the target plate at different angles. The penetration of pre-fragments into the target plate is at high temperature, high pressure, and high strain, accompanied by large plastic deformation and damage. Johnson-cook material model is thus used to describe the dynamic deformation and failure of preformed fragments and target plate materials.

The model considers that the Mises equivalent flow stress of metal material under deformation can be expressed in the form of function$\sigma_y = f(\varepsilon_p, \dot{\varepsilon}_p)$, which can better couple the effects of strain hardening, strain rate hardening and thermal softening. The expression is as follows:

$$\sigma_y = [A + B\varepsilon_p^n][1 + C\, ln(\dot{\varepsilon}_p/\dot{\varepsilon}_0)][1 - T_m^*] \tag{5}$$

where $\varepsilon_p, \dot{\varepsilon}_p$ is the equivalent plastic strain and the equivalent plastic strain rate of the material element, respectively, and $\dot{\varepsilon}_0 = 1s^{-1}$ is the reference strain rate. T^* is a dimensionless temperature parameter; $T^* = \frac{T-T_r}{T_m-T_r}$, T, T_r and T_m is the current temperature, reference room

temperature, and melting temperature of the material, respectively. Parameter A is the quasi-static yield strength of the material; B and n are the dynamic strain hardening correlation coefficient and index of the material, respectively; C is the strain rate hardening coefficient, and m is the thermal softening index. Assuming that 90% of the plastic deformation work is converted into heat, the temperature change of the material element can be obtained by integrating the stress and the equivalent strain increment:

$$\Delta T = 0.9 \int \frac{\sigma d\varepsilon}{\rho C_v} \tag{6}$$

The unit failure of projectile and target materials adopts Johnson-book's cumulative damage failure mode. When the cumulative equivalent plastic strain increment of the material element reaches the critical failure strain, that is,$\sum \Delta\varepsilon_p = \varepsilon^f$, the corresponding material element is deleted in the calculation, and the material is considered to be fracture failure. The expression of ε^f is:

$$\varepsilon^f = [D_1 + D_2\, exp\, D_3\, \sigma^*][1 + D_4 \ln\dot{\varepsilon}^*][1 + D_5 T^*] \tag{7}$$

where $\sigma^* = \sigma_m/\sigma_{eff}$ is the dimensionless ratio of hydrostatic pressure to the equivalent plastic stress, and $D_1 - D_5$ are material constants.

3.2. Eroding single surface

Erosion contact type is set. The muzzle velocity of the projectile is 1300m/s; the material is tungsten alloy, and the thickness of the target plate is 6mm thick steel plate. The relevant parameters of the material model of tungsten alloy and armor steel are given in [20-22], as shown in Table 4.

Table 4. J-C material model parameters of tungsten alloy and 603 steel (cm-g- μ s)

	tungsten alloy	**603 steel**
$\boldsymbol{E}$**/MPa**	410	206
$\boldsymbol{G}$**/MPa**	120	81.4
$\boldsymbol{\rho}$	17.9	7.83
$\boldsymbol{v}$	0.28	0.33
$\boldsymbol{A}$**/Mbar**	0.01510	0.0012
$\boldsymbol{B}$**/Mbar**	0.00177	0.0051
$\boldsymbol{n}$	0.12	0.26
$\boldsymbol{C}$	0.016	0.014
$\boldsymbol{m}$	1.00	1.03
$\boldsymbol{T_m}$**/K**	1723	1793
$\boldsymbol{T_r}$**/K**	293	293
$\boldsymbol{C_v}$**/(J·kg^{-1}·K)**	134	477
$\boldsymbol{D_1}$	2.0	2.0

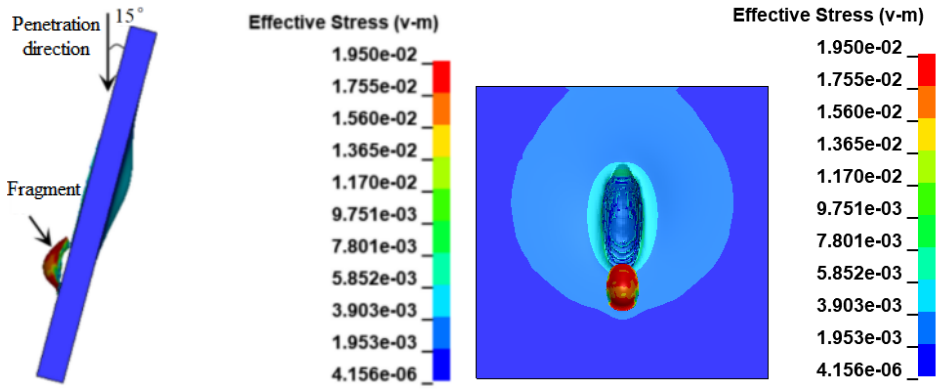
Penetration direction
15°
Fragment
Effective Stress (v-m)
1.950e-02
1.755e-02
1.560e-02
1.365e-02
1.170e-02
9.751e-03
7.801e-03
5.852e-03
3.903e-03
1.953e-03
4.156e-06
Effective Stress (v-m)
1.950e-02
1.755e-02
1.560e-02
1.365e-02
1.170e-02
9.751e-03
7.801e-03
5.852e-03
3.903e-03
1.953e-03
4.156e-06

(a) 15°

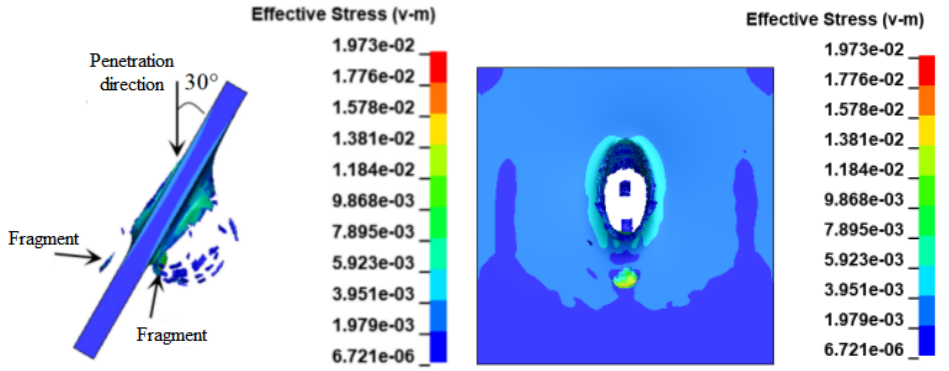
Penetration direction
30°
Fragment
Fragment
Effective Stress (v-m)
1.973e-02
1.776e-02
1.578e-02
1.381e-02
1.184e-02
9.868e-03
7.895e-03
5.923e-03
3.951e-03
1.979e-03
6.721e-06
Effective Stress (v-m)
1.973e-02
1.776e-02
1.578e-02
1.381e-02
1.184e-02
9.868e-03
7.895e-03
5.923e-03
3.951e-03
1.979e-03
6.721e-06

(b) 30°

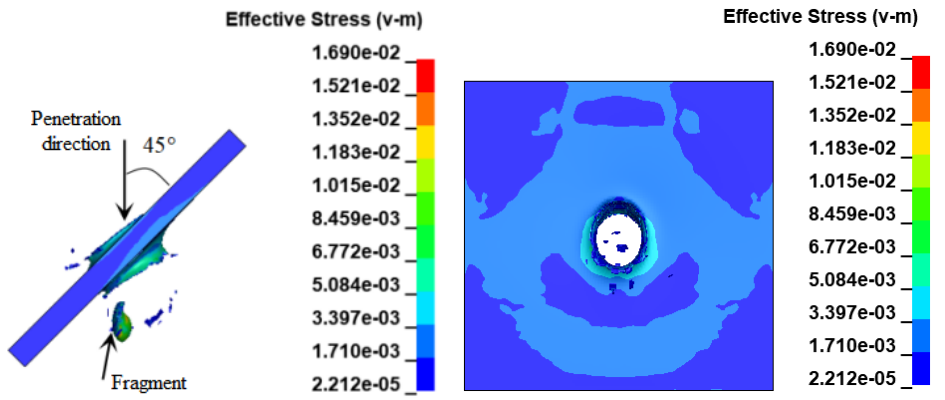
Penetration direction
45°
Fragment
Effective Stress (v-m)
1.690e-02
1.521e-02
1.352e-02
1.183e-02
1.015e-02
8.459e-03
6.772e-03
5.084e-03
3.397e-03
1.710e-03
2.212e-05
Effective Stress (v-m)
1.690e-02
1.521e-02
1.352e-02
1.183e-02
1.015e-02
8.459e-03
6.772e-03
5.084e-03
3.397e-03
1.710e-03
2.212e-05

(c) 45°

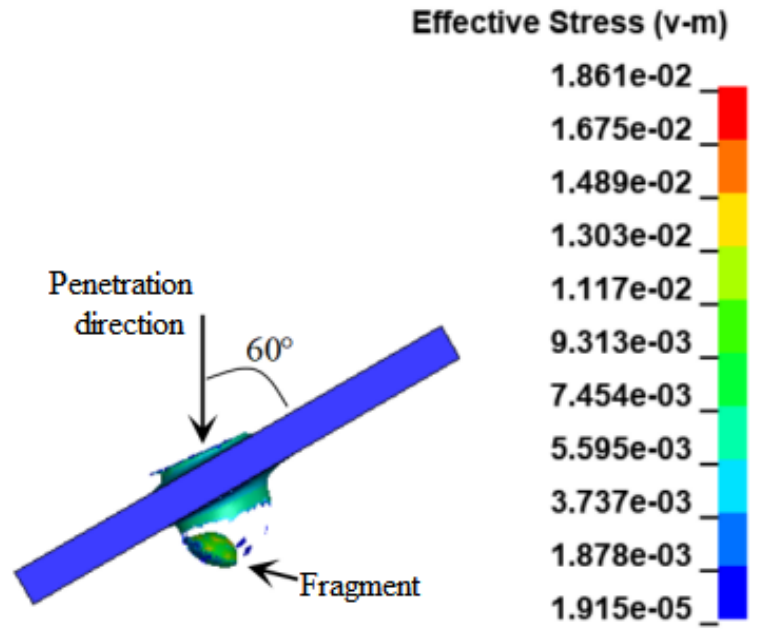
Effective Stress (v-m)
1.861e-02
1.675e-02
1.489e-02
1.303e-02
1.117e-02
9.313e-03
7.454e-03
5.595e-03
3.737e-03
1.878e-03
1.915e-05
Penetration direction
60°
Fragment

(d) 60°

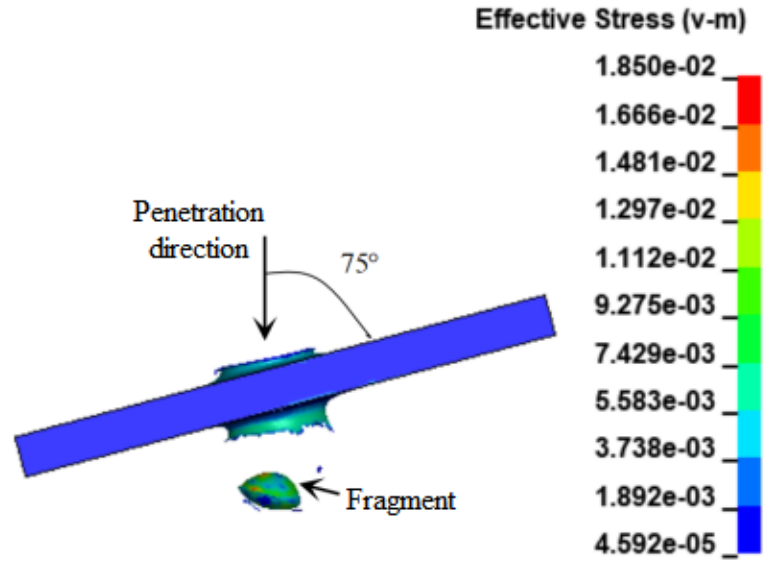
Effective Stress (v-m)
1.850e-02
1.666e-02
1.481e-02
1.297e-02
1.112e-02
9.275e-03
7.429e-03
5.583e-03
3.738e-03
1.892e-03
4.592e-05
Penetration direction
75°
Fragment

(e) 75°

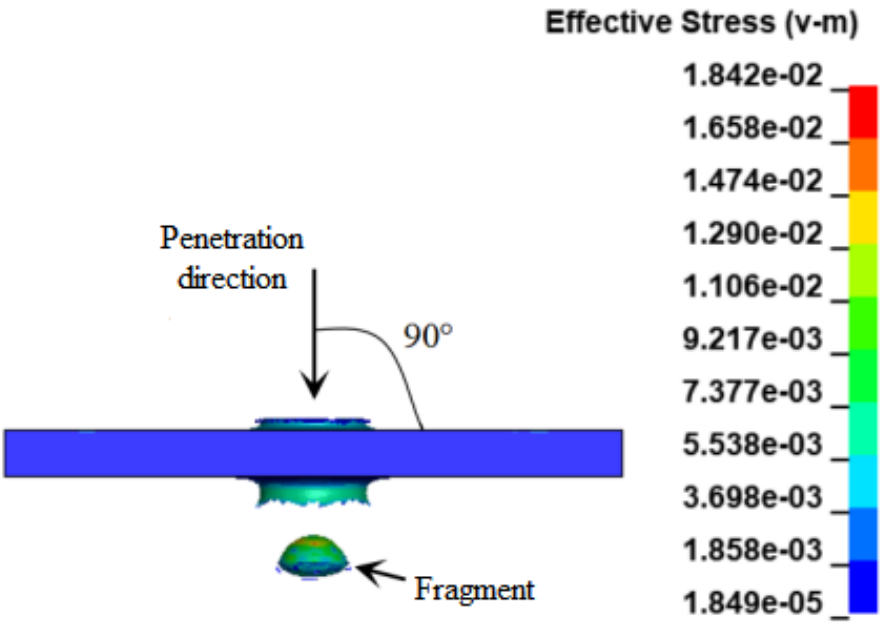

(f) 90°

Fig. 9. Damage effect of penetrating the target plate at different angles

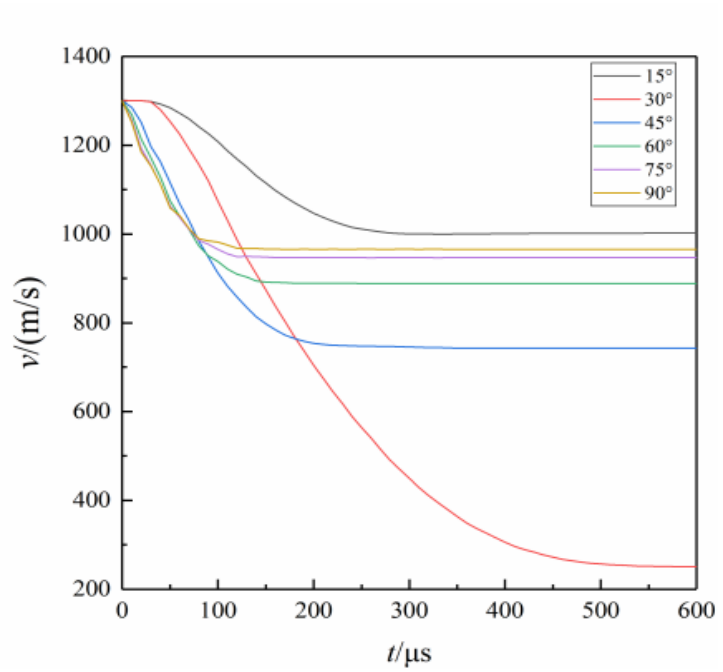

Fig.10. Residual velocity of fragment at different penetration angles

Fig. 9 shows the damage to the target plate at different penetration angles. When the target plate material is 604 steel, the thickness is 6mm, and the penetration angle is 15°. At this time, the spherical projectile cannot penetrate the target plate, and the contact part between the projectile and the target plate breaks. Some spherical projectiles are embedded in the target plate, and the other half of the non-contact projectile part jumps. When the penetration angle is more than 30°, the spherical projectile can well destroy the target, and some spheres are still embedded in the target. As the penetration angle increases, the fragmentation degree of the projectile decreases; the sphere embedded in the target plate decreases, and the damage pit area decreases. The residual velocity of corresponding fragment after penetration is extracted as shown in Fig. 10. When the penetration angle is 15°, the spherical projectile bounces off. When the penetration angle is more than 30°, the residual velocity of the projectile decreases with the decrease of the penetration angle. The experimental results show that the tungsten alloy pre-fragment warhead can basically destroy the steel target. Only when the penetration angle is small, the ability to destroy the target plate will be reduced, and the tungsten alloy fragments that penetrate the target plate will also be reduced.

4. CONCLUSION

The simulation and experimental results show that the tungsten alloy pre-fragment missile warhead can be well formed and destroyed. The following conclusions are drawn:

1) The tungsten alloy per-fragment warhead can form a lot of skin damage after initiation. The velocity of skin damage is relatively high near the initiation point and low at the far initiation point. At the same time, the fitting results of the theoretical formula of the contrast velocity attenuation are consistent with the experimental results. The attenuation of the skin-breaking velocity is small in a certain distance.
2) The tungsten alloy per-fragment can well destroy the steel target. When the damage angle is greater than 30°, it can penetrate the 6mm steel target. As the penetration angle increases, the residual velocity of the tungsten alloy fragment is high.

ACKNOWLEDGMENTS

The work was supported by the Science research funding project of Liaoning Provincial Department of Education (No. LJKZ0269), and Cultivation and Construction Project of High-level Achievement ofShenyang Ligong University, and Guangxuan Talents of Shenyang Ligong University, and Guangxuan Teams of Shenyang Ligong University.

REFERENCES

[1] Baek, J.H., Lee, S.P., Lee, Y.J., Kim, S.U., Design of Subminiaturized Natural Fragment Warhead based on the Analysis of Warhead Effectiveness. Journal of the Korean Society for Precision Engineering, 2018, 35(10): p. 933-941.

[2] Dhote, K. D., Murthy, K. P. S., Rajan, K. M., & Sucheendran, M. M., Quantification of projection angle in fragment generator warhead. Defence Technology, 2014, 10(2): p. 177-183.

[3] Zhao, J., Fu, J.P., Chen, Z.G., Guo, Z.Y., Zhang, J., Zheng, C.J., Analysis of Forming and Spreading of Pre-Formed Fragment Warhead. Journal of Ordnance Equipment Engineering, 2019, 40(12): p. 62-66.

[4] Wei, J.F., Jiao, Q.J., Wu, C., Experiment and Simulation on Premade Fragment Warhead. Journal of Projectiles, Rockets, Missiles and Guidance, 2004, 24(3): p. 39-41+45.

[5] Dhote, K. D., & Deodhar, R. S., Effect of fragment dispersion on damage assessment of a directional fragment generator. International Journal of Damage Mechanics, 2017, 27(4): p. 568-577.

[6] Dhote, K. D., Murthy, K. P., Rajan, K. M., & Sucheendran, M. M., Statistics of Fragment Dispersion by Explosion in a Fragment Generator Warhead. Central European Journal of Energetic Materials, 2016, 13(1): p. 183-197.

[7] Mei, R.B., Feng, T.Y., Huang, B., Zhang, H.J., Li, M.Y., Zhang, B.H., Numerical simulation and structural optimization of cylindrical prefabricated fragments under explosion impact. Journal of Plasticity Engineering, 2022, 29(2): p. 197-203.

[8] Mao, L., Jiang, C.L., Yan, H.X., Zhang, L.Y., Wang, C., Numerical simulation and experiment on aim able warhead of premade fragment. Journal of Vibration and Shock, 2012, 31(13): p. 66-70+75.

[9] Roisman, I. V., Weber, K., Yarin, A. L., Hohler, V., & Rubin, M. B., Oblique penetration of a rigid projectile into a thick elastic–plastic target: theory and experiment. International Journal of Impact Engineering, 1999, 22(7): p. 707-726.

[10] Zhang, J., Xu, Y.X., Liu, T.L., Zhang, P., Oblique Penetration effect of a Tungsten Ball on High Hardness Steel. Explosion and Shock Waves, 2022, 42(2): p. 71-82.

[11] Ma, Y., He, Y., Wang, C.T., He, Y., Guo, L., Response behavior of double layer tungsten fragments under detonation loading. Journal of Northwestern Polytechnical University, 2022, 40(4): p. 819-828.

[12] Rittel, D., & Weisbrod, G., Dynamic fracture of tungsten base heavy alloys. International Journal of Fracture, 2001, 112: p. 87-98.

[13] Clayton, J., Dynamic plasticity and fracture in high density polycrystals: constitutive modeling and numerical simulation. Journal of the Mechanics and Physics of Solids, 2005, 53(2): p. 261-301.

[14] Yu, Z., & Shi, D., Study on Fragment Velocity Measurement Technology of Prefabricated Fragment Warhead. 2018 3rd International Conference on Materials Science, Machinery and Energy Engineering, 2018, p. 304-308.

[15] Wang, Z., Yin, J., Li, X., & Yi, J., Effect of Wood Medium on Dispersion Parameters of Prefabricated Spherical Fragments in Forest. Applied Sciences, 2022, 12(22): p. 11333.

[16] Bai, C., Wang, H., & Feng, C., Analysis of criteria for assessing safety distance for focused warhead fragments based on CDEM. Mathematical Problems in Engineering, 2019, 2019: p. 8735481.

[17] Wang, Y., Li, W., Zhu, G., & Li, W., Oblique Penetration of a Circular Pipe Target by a Prefabricated Fragment. International Journal of Structural Stability and Dynamics, 2019, 19(10): p. 1950119.

[18] Wang, H., Bai, C., Feng, C., Xue, K., & Zhu, X., An efficient CDEM-based method to calculate full-scale fragment field of warhead. International Journal of Impact Engineering, 2019, 133: p. 103331.

[19] Zuo, T., Study on the Low Collateral Damage Performance of CERP Shell Structure. Beijing Institute of Technology, 2016.

[20] Wang, M., Yang, M.C., Luo, R.M., Tang, E.L., Numerical Simulation on the Adiabatic Shear Failure at Cratering Stage for Tungsten Alloy Long Rod Penetrator Piercing into Armor. Journal of Vibrtion and Shock, 2016, 35(18): p. 111-116.

[21] Cheng, C., Xu, L., Pang, Z., Du, Z., Wang, M., & Chen, X., Fragmentation characteristics of PELE shell perforating thin metal target plate. Mechanics of Advanced Materials and Structures, 2020, 29(8): p. 1198-1209.

[22] Cheng, C., Du, Z. H., Chen, X., Xu, L. Z., Du, C. X., Han, J. L., & Wang, X. D., Damage of multi-layer spaced metallic target plates impacted by radial layered PELE. Defence Technology, 2020, 16(1): p. 201-207.